RSC Advances

PAPER

View Article Online
View Journal | View Issue

Cite this: *RSC Adv.*, 2018, **8**, 33208

Inheritance of spherical morphology and optimization of assembled structures during preparation of $LiMnPO_4$ cathodes for high electrochemical properties

Xiaoliang Pan, *[a] Zhi Gao,[a] Lijun Liu,[b] Fan Xiao,[a] Fen Xiao,[a] Shikun Xie[a] and Yonghong Liu[a]

Received 9th July 2018
Accepted 6th September 2018

DOI: 10.1039/c8ra05832f

rsc.li/rsc-advances

Microspherical structures of cathodes facilitate high tap densities and good cycling stabilities, but their inferior rate capabilities due to low surface permeability for the electrolyte, remains a hurdle. An effective strategy to address this issue would be the optimization of the assembled microspheres structure. In this work, $LiMnPO_4$ hollow microspheres assembled by radially aligned nanoprisms with fully exposed (010) facets are prepared by the solvothermal method using Li_3PO_4 as the self-sacrificed templates to improve the rate capability. By simply varying ammonium based salts during the solvothermal reaction, the nanoprisms-randomly assembled and the wedges-radially assembled microspheres are also fabricated. A plausible formation mechanism is carefully proposed. When the three kinds of microspheres are evaluated by charge/discharge measurements, their electrochemical properties are highly dependent on the variation of the assembled structures. In particular, microspheres with radially aligned nanoprisms exhibit high rate capabilities, delivering discharge capacities of 125 mA h g^{-1} at 1C and 113 mA h g^{-1} at 2C. These results originate from the unique structure of the microspheres, which not only ensures rapid electrolyte penetration to the interior of the shells due to the radial pore channels, but also guarantees fast Li^+ insertion into the nanoprisms owing to their fully exposed (010) facets.

Introduction

Lithium-ion batteries with high energy and power densities as well as long cycle lives have been widely explored to meet the increasing energy storage demands for consumer electronics, electric vehicles, and stationary power stations.[1–3] As a crucial component, cathode materials strongly determine the performance and the cost of lithium-ion batteries. To replace the highly priced and toxic cobalt based cathodes, tremendous efforts have been undertaken to develop electrochemically active cathodes which are inexpensive and non-toxic including $LiMn_2O_4$, $LiMPO_4$ (M = Mn and Fe).[4,5] Among potential cathode materials, $LiMnPO_4$ has inspired extensive research interest due to its natural abundance, high environmental friendliness, excellent cycling stability and superior intrinsic safety.[6–9] Despite these merits, it suffers from poor rate capabilities due to low electrical conductivity and slow lithium ion diffusion kinetics.[10–12]

In view of the above problems, the present research suggests alternative routes to enhance the rate capability of the $LiMnPO_4$ cathode. Notably, it was reported that electrochemical activities varied with the nature of the crystal facet for the electrode, and specific crystal orientations have been demonstrated to be effective in improving their properties.[13–15] For $LiMnPO_4$ cathodes, the (010) crystal facet facilitates Li^+ insertion/extraction. So crystals with fully exposed (010) facets can significantly increase the proportion of electrochemically active sites, which can effectively enhance the rate performance.[16] For example, single-crystalline $LiMPO_4$ (M = Mn, Fe, Co) nanosheets with significant (010)-facet exposure demonstrated a greatly improved rate capability;[17] well-dispersed $LiMnPO_4$ plates with a large degree of exposed (010) facets showed an enhanced rate capability.[18]

In addition to the rate capability, the cycling stability and the tap density are also rather important for practical applications.[19] Particularly, hollow microspheres have proved to be suitable architectures for realizing high-rate, long-life and close-packing battery electrodes. Hollow microspheres can offer the exceptional advantages afforded by both the nanoscale primary subunits and the micron-sized assemblies.[20] Moreover, the hollow interior can provide extra void space for increased contact area with the electrolyte, and accordingly offer more active facets for Li^+ insertion.[21] In addition, compared to hollow microspheres with irregular pore channels, the hollow

---

[a] *School of Mechanical Engineering, Jinggangshan University, Jian, 343009, China. E-mail: xiaoliang_pan@163.com; Fax: +86 7968100455; Tel: +86 15779627062*

[b] *School of Chemistry and Chemical Engineering, Jinggangshan University, Jian, 343009, China*

microspheres with radial pore channels can achieve rapid electrolyte penetration not only at the exterior surface but also within the large interior surface, which ensures faster charge transfer.[22]

In this regard, various methods have been developed including solution processing,[23] hydrothermal reaction,[24,25] solvothermal treatment,[26,27] etching approach,[28] and templating routes[29] to controllably synthesize novel hollow microspheres. Among them, the sacrificial template method has been demonstrated to be a facile and straightforward process to prepare hollow microspheres because of the high controllability of its physical properties, such as the size and the morphology of the samples.[30] For example, hollow Ge microspheres constructed by interconnected nanoparticles were prepared by reduction of GeO_2 in a molten-salt system, which exhibited good electrochemical Li-storage performance.[31] $x Li_2MnO_3 \cdot (1-x) LiNi_{1/3}Co_{1/3}Mn_{1/3}O_2$ hollow microspheres were fabricated using $Co_yMn_{3-y}O_4$ microspheres as self-sacrificial templates; they exhibited a high specific capacity, long cycling life, and a good rate capability.[32] Fe_3S_4 hollow spheres using Fe_3O_4 colloidal spheres as sacrificial templates were composed of many fine primary magnetite nanocrystals, which showed highly reversible capacity.[33] Hollow $LiFePO_4$ microspheres consisting of the nanoparticles were synthesized by a solvothermal method using spherical Li_3PO_4 microspheres as the self-sacrificed template, delivering high charge–discharge capacities.[29] $Li_4Ti_5O_{12}$ hollow spheres using SiO_2@a-TiO_2 core–shell spheres as the template were composed of ~8 nm nanoparticles, and achieved remarkable rate capability with stable long-term capacity retention.[34]

From the above mentioned results, we observe that the striking features of the hollow morphologies can be inherited from the sacrificial templates. However, the structure of the shells and the orientation of the subunits are not further improved. In this regard, hollow superstructures with radial pore channels for the shells and fully exposed active facets for the subunits might be a good strategy to meet the growing need of high rate capacities for lithium-ion batteries.

Herein, $LiMnPO_4$ hollow microspheres assembled by radially aligned nanoprisms with exposure of (010) facets were synthesized by a simple solvothermal method using Li_3PO_4 hollow microspheres as the self-sacrificed templates. The effects of ammonium based salts on the assembled structures of the microspheres were elucidated and a plausible formation mechanism was proposed. The electrochemical performances were quantitatively compared for microspheres with distinct shell structures or subunit shapes.

Experimental

Materials syntheses

All chemicals in the present experiment were analytical-grade reagents and used as received without further purification.

Li_3PO_4 templates were prepared by a precipitation method. In a typical synthesis, 21 mmol $C_2H_3O_2Li \cdot 2H_2O$, 7 mmol $NH_4H_2PO_4$, 80 mmol NaOH were dissolved in 32 mL deionized water and 8 mL diethylene glycol, and magnetically stirred at room temperature for 30 min. The as-obtained precipitate was alternately washed with deionized water and ethanol several times by centrifugation, and dried at 60 °C overnight in air to obtain Li_3PO_4 precursors.

To prepare $LiMnPO_4$ samples, a solvothermal treatment was performed. 5 mmol Li_3PO_4, 5 mmol $(C_2H_3O_2)_2Mn \cdot 4H_2O$, and 2 mmol $NH_4H_2PO_4$ were dispersed in a mixed solvent of 20 mL deionized water and 20 mL ethylene glycol. Then, the resulting mixture was magnetically stirred at ambient conditions for 30 min, transferred to a Teflon-lined autoclave with a capacity of 50 mL, and kept in an oven at 180 °C for 4 h. After cooling to room temperature, the precipitate was collected and washed with water and ethanol several times. Finally, $LiMnPO_4$ hollow microspheres were obtained.

In order to investigate the effects of ammonium based salts on the assembled structures of $LiMnPO_4$ microspheres, controlled experiments were performed where 1 mmol $(NH_4)_2C_2O_4 \cdot H_2O$ and 2 mmol NH_4Cl instead of 2 mmol $NH_4H_2PO_4$ were used as the reagents to maintain NH_4^+ levels, while the other conditions were kept unchanged.

Materials characterizations

XRD patterns of the samples were recorded on an X-ray powder diffractometer (Rigaku D/max-rA diffractometer, Cu Kα radiation, $\lambda = 1.5406$ Å) and were compared with Joint Committee on Powder Diffraction Standards (JCPDS) cards. Morphologies and structures of the samples were investigated by field emission scanning electron microscopy (FE-SEM, FEI Quanta 200F), transmission electron microscopy (TEM, JEOL JEM-3200FS) and high-resolution TEM analyses.

The electrochemical properties were evaluated with a Land-CT2001A battery test system (Jinnuo Wuhan Corp., China) by cycling of 2032 coin-type cells. The cells were assembled in an argon-filled glove box by sequentially stacking together the working electrode, a Celgard 2400 polypropylene membrane and a pure lithium disk in a solution of ethylene carbonate/dimethyl carbonate (EC and DMC, 1 : 1 in volume) electrolyte containing 1 M $LiPF_6$. To improve conductivity, the as-fabricated $LiMnPO_4$ samples were coated with carbon by mixing with sucrose and heating at 700 °C for 2 h. To fabricate the working electrode, the $LiMnPO_4$, Super P and polyvinylidene fluoride were thoroughly mixed together with a weight ratio of 70 : 20 : 10, respectively, to obtain the homogeneous slurry. Then, the slurry was cast onto an Al foil. The foil was dried at 60 °C for 12 h and then was cut into disks. The disks were dried at 120 °C under vacuum for 10 h to finally obtain the working electrode. The cells were charged at galvanostatic mode to 4.5 V, held at 4.5 V until 0.05C, and then discharged at galvanostatic mode to 2.4 V at various current densities. Electrochemical impedance spectroscopy (EIS) was performed on a CHI660E electrochemical workstation (Chenhua Instruments Shanghai Inc., China), and the ac voltage signal of 5 mV was used over a frequency range from 0.01 to 100 kHz. In addition, all the electrochemical measurements were carried out at room temperature.

Results and discussion

Characterizations of microspheres

XRD patterns of the as-prepared samples are shown in Fig. 1. Fig. 1a presents the XRD pattern of the templates. The obtained diffraction peaks correspond well to the standard patterns of the Li_3PO_4 phase without any distinct impurity (JCPDF card no. 15-0760), and the broad peaks indicate that Li_3PO_4 is crystallized at the nanoscale. The XRD patterns of $LiMnPO_4$ samples fabricated with different ammonium based salts are shown in Fig. 1b–d. For all the samples, the obtained diffraction peaks agree well with the orthorhombic *Pnmb* space group based on the olivine structure (JCPDS file no. 74-0375); no significant impurity peaks are detected, denoting the high purity of the $LiMnPO_4$ phase.

The morphology and structure of the as-prepared Li_3PO_4 templates were systematically characterized. As shown in Fig. 2a and b, the Li_3PO_4 templates display uniform spherical morphology with an average diameter of about 2 μm. As seen from the cross section of the broken microsphere in Fig. 2c, it can be clearly observed that the microsphere consists of the hollow cavity and a thin shell with a thickness of about 400 nm. As observed from the magnified SEM image in Fig. 2d, it can be found that the surface of the microsphere is densely and firmly constructed by numerous nanoparticles. The TEM image in Fig. 2e further reveals that the microspheres display a porous structure, and large cores can be clearly observed at the center of the microspheres. HRTEM image in Fig. 2f shows that the interplanar distance is 0.45 nm, which corresponds to the (011) facet of Li_3PO_4 crystals.

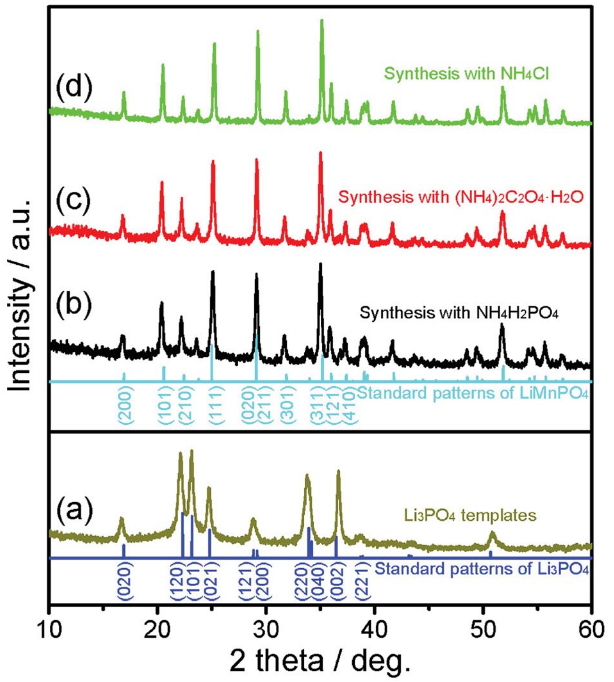

Fig. 1 XRD patterns of Li_3PO_4 templates (a) and $LiMnPO_4$ samples synthesized with $NH_4H_2PO_4$ (b), $(NH_4)_2C_2O_4\cdot H_2O$ (c), and NH_4Cl (d).

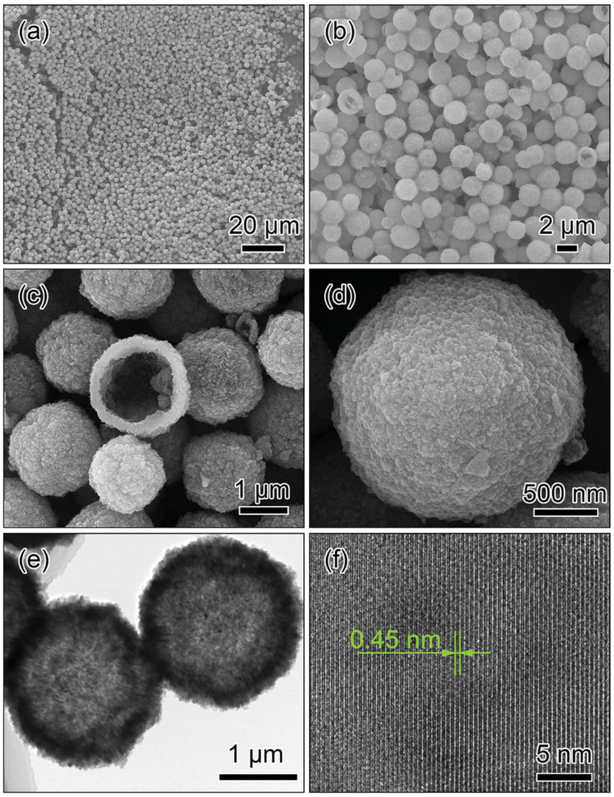

Fig. 2 SEM (a–d), TEM (e) and HRTEM (f) images of Li_3PO_4 templates.

Fig. 3 shows the SEM, TEM and HRTEM images of the $LiMnPO_4$ sample fabricated with $NH_4H_2PO_4$. Low-magnification SEM images (Fig. 3a and b) clearly demonstrate that the spherical morphology is maintained after the solvothermal process. The magnified image in Fig. 3c reveals that the microsphere consists of numerous nanoprisms of about 500 nm in length. Interestingly, these nanoprisms align radially, attach each other through the ends and assemble into the urchin-like microspheres (hereafter designated as radial-prisms microspheres), resulting in the formation of abundant straight and radially aligned pore channels in the shells. TEM images in Fig. 3d and e reveal the contrast differences between the interiors and the edges of the microspheres, confirming that radial-prisms microspheres possess a hollow structure. HRTEM imaging was performed at the edge of the nanoprism to further reveal the crystal structure as shown in Fig. 3f. Two sets of regular lattice fringes can be observed. The one perpendicular to the length direction of the nanoprism presents a lattice spacing of 0.47 nm and corresponds to the (001) facet, suggesting that the nanoprism grows preferentially along the [001] direction; the other one parallel with the length direction of the nanoprism exhibits a lattice spacing of 0.61 nm and is matched with the (100) facet. Consequently, it is found that the surfaces (parallel to the figure plane) of the nanoprism fully expose the (010) facets of orthorhombic $LiMnPO_4$, indicating that the [010] direction is one of the short axes of the nanoprism with a thin thickness. The inset of Fig. 3f is the corresponding fast Fourier transform (FFT) pattern, confirming the monocrystalline nature of the $LiMnPO_4$ nanoprism.

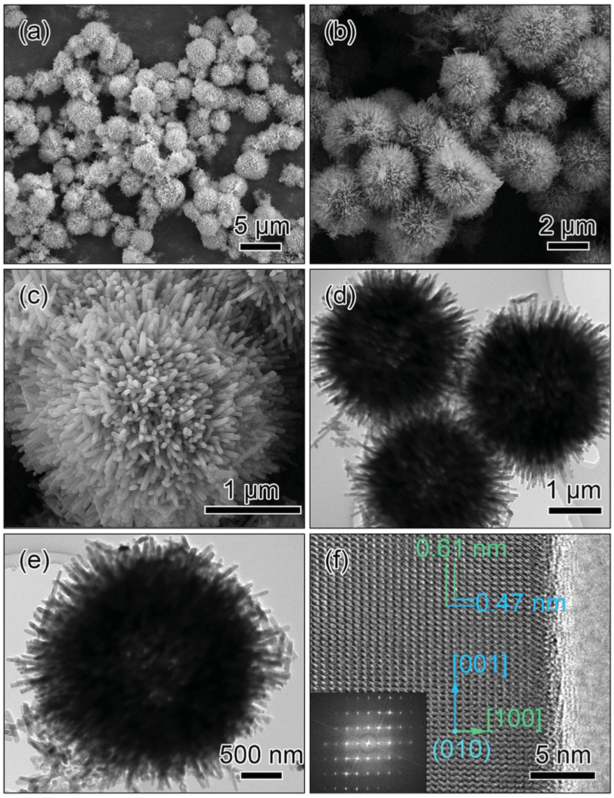

Fig. 3 SEM (a–c), TEM (d and e) and HRTEM (f); the inset: fast Fourier transform of the lattice structure in (f) images of the microspheres assembled by the radially aligned nanoprisms (radial-prism microspheres).

The structure of the microspheres with voids in the cores and radial pore channels in the shells ensures easy penetration of the electrolyte. In addition, the orientation of the nanoprisms with fully exposed (010) facets as well as the thinness along the [010] direction guarantees fast insertion for lithium ions, all of which are crucial for electrochemical reactions at the cathode in lithium-ion batteries.

Control of assembled structures of $LiMnPO_4$ microspheres

In order to understand the function of ammonium based salts on the structure of the final sample in the solvothermal process, controlled experiments were conducted where 1 mmol $(NH_4)_2C_2O_4\cdot H_2O$ and 2 mmol NH_4Cl instead of 2 mmol $NH_4H_2PO_4$ were used as the reagents to maintain NH_4^+ levels, while the other conditions were kept identical as those for the fabrication of the radial-prisms microspheres.

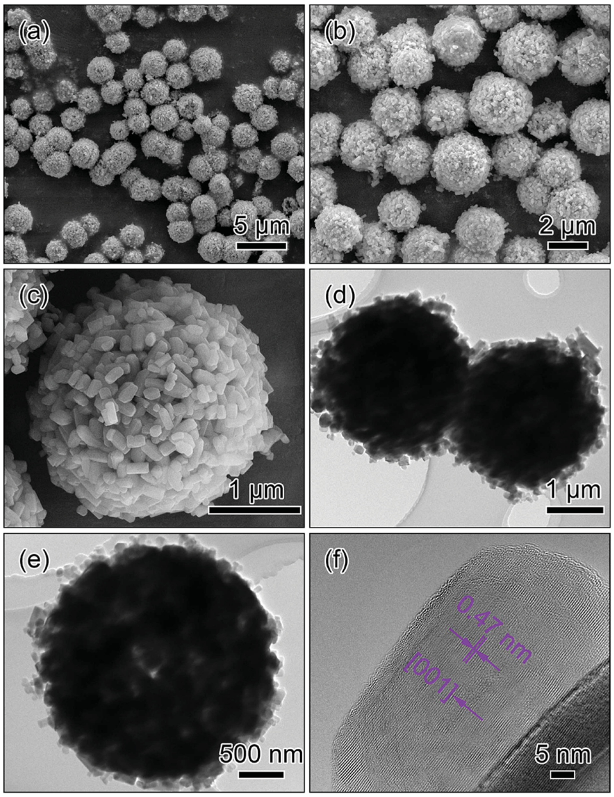

Fig. 4 SEM (a–c), TEM (d and e) and HRTEM (f) images of the microspheres assembled by the randomly agglomerated nanoprisms (random-prisms microspheres).

Fig. 4 displays the SEM, TEM and HRTEM images of the $LiMnPO_4$ sample prepared with $(NH_4)_2C_2O_4\cdot H_2O$. As shown in Fig. 4a and b, the sample comprises monodisperse microspheres with an average diameter of about 2.6 μm, exhibiting the inherited morphology from the Li_3PO_4 template. From the highly magnified SEM image in Fig. 4c, it is observed that the microsphere is randomly agglomerated by short nanoprisms with an average length of ~240 nm (hereafter designated as random-prisms microspheres). Although random-prisms microspheres are not very easy for the electron beam to transmit, mainly due to their randomly oriented structures and block sizes along the diameter direction, the slight contrast in the TEM images in Fig. 4d and f can confirm that random-prisms microspheres have a hollow porous structure. The HRTEM image in Fig. 4f reveals that the nanoprism has an interplanar distance of 0.47 nm, which can be indexed to the (001) facet of $LiMnPO_4$.

Fig. 5 presents the SEM, TEM and HRTEM images of the $LiMnPO_4$ sample synthesized with NH_4Cl. The SEM images in Fig. 5a and b show that the spherical morphology is maintained after the solvothermal reaction. From the magnified image in Fig. 5c, it can be observed that the microsphere comprises radially grown wedge-like crystals, exhibiting an urchin-like morphology (hereafter designated as radial-wedges microspheres). TEM images in Fig. 5c and d display that there is a brighter contrast at the center of the microspheres, confirming that the radial-wedges microspheres have a hollow interior. The HRTEM image in Fig. 5f shows that the wedge-like crystal presents perfect crystallinity with the interplanar distance of 0.28 nm, corresponding to the (031) facet of $LiMnPO_4$.

Formation mechanism of $LiMnPO_4$ microspheres

Based on the above observations, it can be safely concluded that the change in ammonium based salts can lead to variations in the shell structures and crystal orientations of the $LiMnPO_4$ microspheres in the solvothermal process. We can

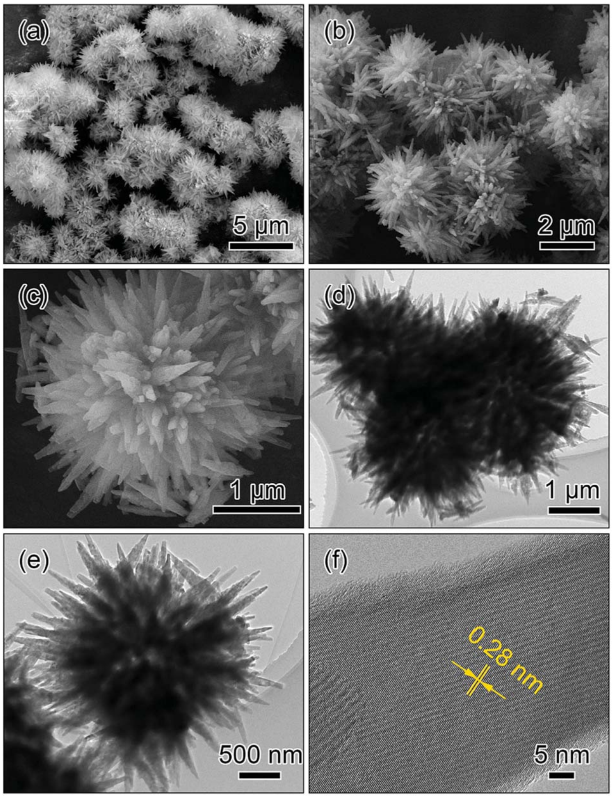

Fig. 5 SEM (a–c), TEM (d and e) and HRTEM (f) images of the microspheres assembled by the radially aligned wedges (radial-wedges microspheres).

subsequently clarify the correlation between the ammonium based salts and the assembled structures.

Firstly, Li_3PO_4 can readily dissolve under acidic conditions originating from ammonium based salts,[35–37] generating Li^+ cations and PO_4^{3-} anions in the solution. As the pH value of the solution decreases, more Li^+ cations and PO_4^{3-} anions may be released from Li_3PO_4 into the solution, providing conditions for a higher nucleation rate and a faster growth of the $LiMnPO_4$ crystals. Therefore, the nucleation and growth rates in the solution with $NH_4H_2PO_4$ or NH_4Cl are higher than those in the solution with $(NH_4)_2C_2O_4 \cdot H_2O$.

Secondly, the Mn^{2+} concentration close to the Li_3PO_4 microspheres is lower than that of the ones away from the Li_3PO_4 microspheres due to the expense for the formation of $LiMnPO_4$ crystals. Meanwhile, the diffusion rate of Li^+ is larger than that of Mn^{2+} in solution. For the solvothermal process with $NH_4H_2PO_4$ or NH_4Cl, the higher growth rate of $LiMnPO_4$ crystals requires more Mn^{2+} to be available for the reaction. However, a low concentration and slow diffusion rate of Mn^{2+} close to the Li_3PO_4 microspheres cannot afford rapid growth of $LiMnPO_4$ crystals, eventually resulting in the radially aligned growth and the urchin-like morphology. Conversely, the solvothermal synthesis with $(NH_4)_2C_2O_4 \cdot H_2O$ may undergo a slow growth process, and Mn^{2+} concentration close to the Li_3PO_4 microspheres can gradually increase due to the concentration gradient, finally leading to the casually oriented growth and randomly agglomerated morphology.

Thirdly, different crystallographic orientations of the $LiMnPO_4$ crystals can be directly associated with various surface energy of facets and selective absorption of anions during the further crystallization process. According to the previous studies,[17,38,39] {010} facets are low energy surfaces, indicating that these facets can contribute to the dominant surface area of the final morphologies. Additionally, Cl^- could selectively absorb on special facets, stabilizing them and promoting the oriented growth of the crystals, which can also be identified in other previous studies.[22,40,41] Consequently, for preparations with $NH_4H_2PO_4$ and $(NH_4)_2C_2O_4 \cdot H_2O$, the prism-like crystals with exposed {010} facets can be readily obtained owing to the lower surface energy; for the fabrication with NH_4Cl, chloride anions could preferentially absorb on high-index facets, which helps to cultivate the wedge-like crystals. On the basis of the above discussion, the strategy to control the assembled structures of the hollow $LiMnPO_4$ microspheres is schematically illustrated in Fig. 6.

Electrochemical performance

The electrochemical properties of the three microspheres were evaluated by assembling CR2032 coin-type cells. The cells were charged at galvanostatic mode to 4.5 V, held at 4.5 V until 0.01C ($1C = 170$ mA g^{-1}), and then discharged at galvanostatic mode to 2.4 V at room temperature.

Fig. 7a–c show the charge/discharge curves of the three microspheres. All of the microspheres clearly display a broader potential plateau around 4.1 V corresponding to Li^+ insertion/extraction. In detail, radial-prisms microspheres exhibit discharge capacities of 162, 156, 147, 136, 125 and 113 mA h g^{-1} at 0.05, 0.1, 0.2, 0.5, 1 and 2C, respectively; random-prisms microspheres deliver discharge capacities of 152 mA h g^{-1} at 0.05C, 145 mA h g^{-1} at 0.1C, 133 mA h g^{-1} at 0.2C, 125 mA h g^{-1} at 0.5C, 115 mA h g^{-1} at 1C and 101 mA h g^{-1} at 2C; radial-wedges microspheres have discharge capacities of 138, 128, 119, 111, 100 and 85 mA h g^{-1} at 0.05, 0.1, 0.2, 0.5, 1 and 2C, respectively. These results indicate that radial-prisms microspheres present higher discharge capacities as cathode material in lithium-ion batteries than those of random-prisms microspheres and radial-wedges microspheres.

To further understand the electrochemical processes of the three microspheres, the plots of the differential capacity (dQ/dV) *vs.* cell voltage (V), reproduced from the initial cycle at 0.05C, are shown in Fig. 7d. For radial-prisms microspheres, a couple of redox peaks at 4.0492 and 4.1853 V can be observed, corresponding to Li^+ insertion/extraction. In comparison, the reduction/oxidation peaks of random-prisms microspheres and radial-wedges microspheres are at 4.0442/4.1871 V and 3.9721/4.2141 V, respectively. Thereby, the separation between the redox peaks of radial-prisms microspheres (136.1 mV) is slightly smaller than that of the random-prisms microspheres (142.9 mV), and slightly exceeds half of that of radial-wedges microspheres (242 mV), indicating that radial-prisms microspheres exhibit lower electrode polarization.

The rate capabilities at high current densities were further investigated as shown in Fig. 8a. The radial-prisms microspheres retain 125, 113, 96 and 68 mA h g^{-1} under 1, 2, 5 and

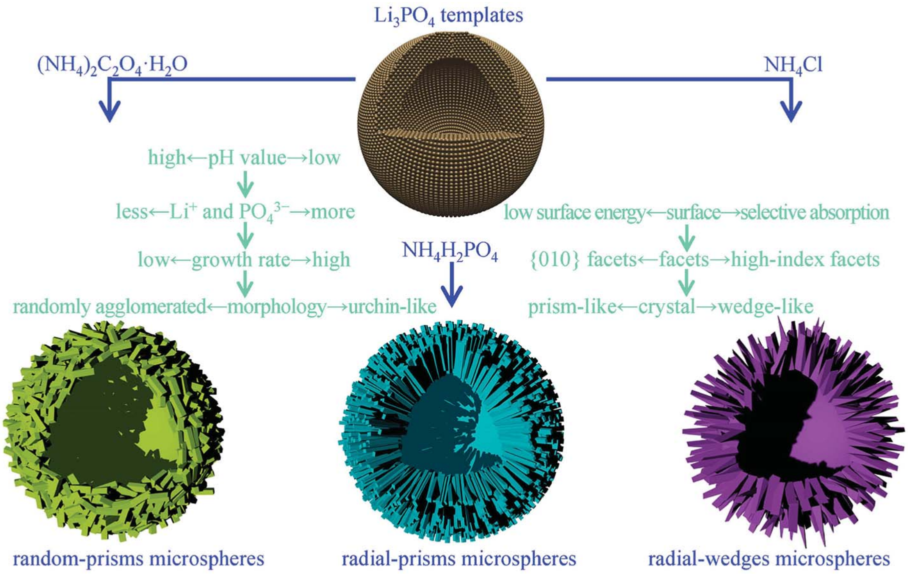

Fig. 6 Schematic illustration of the formation mechanism of the $LiMnPO_4$ microspheres.

10C rates, respectively. When the rate reverts to 1C, the discharge capacity can still remain 125 mA h g^{-1}, demonstrating a good rate performance. In contrast, the discharge capacities of the random-prisms microspheres are 115 mA h g^{-1} at 1C, 101 mA h g^{-1} at 2C, 80 mA h g^{-1} at 5C and 37 mA h g^{-1} at 10C, and the discharge capacities of radial-wedges microspheres only have 100, 84, 69 and 19 mA h g^{-1} at 1, 2, 5 and 10C rates, respectively. It can clearly be noted that the radial-prisms microspheres demonstrate a slower decrease in discharge capacities in comparison with those of the remaining two microspheres as the rates increase. A higher rate capacity suggests better reaction kinetics. These results indicate that radial-prisms microspheres exhibit an enhanced rate performance which could be attributed to the improved kinetics.

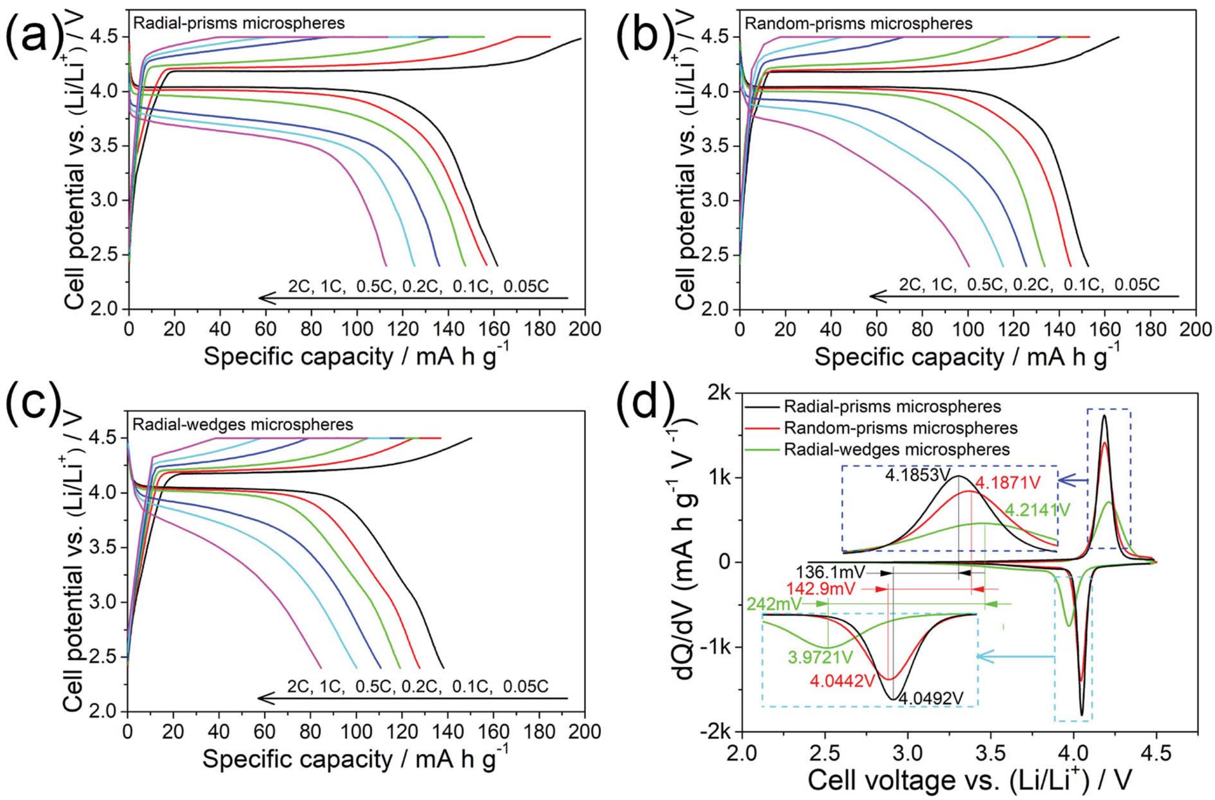

Fig. 7 The charge/discharge curves (a–c) and the dQ/dV *vs.* voltage plots (d) of the three microspheres.

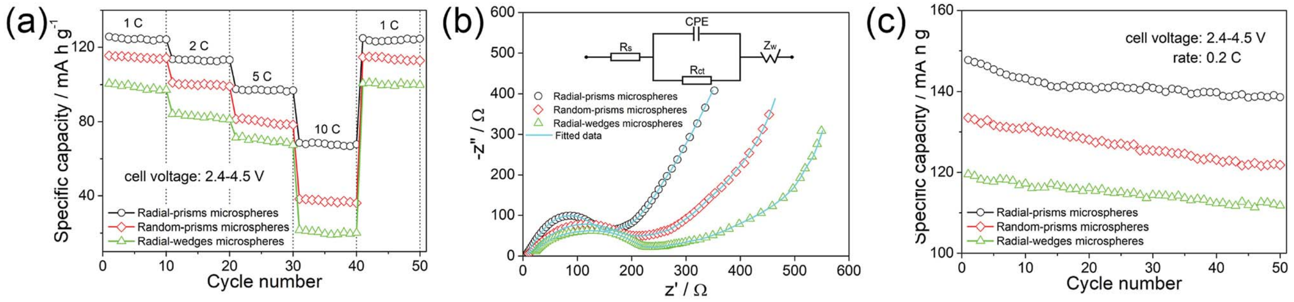

Fig. 8 The rate capabilities (a); the Nyquist plots (b), the inset presents the equivalent circuit; the cycling performances (c) of the three microspheres.

In order to further study the electrochemical kinetics of the three microspheres, electrochemical impedance spectra (EIS) were conducted in the frequency range of 0.01 Hz to 100 kHz after 10 cycles at room temperature. Fig. 8b shows the Nyquist plots of the three microspheres. All the spectra are composed by a quasi-semicircle in the high-medium-frequency range and a straight sloping line in the low frequency range. Generally, the quasi-semicircle is mainly related to the charge transfer resistance at the electrode–electrolyte interface, while the straight sloping line is assigned to Warburg impedance of Li^+ diffusion in the electrode.[42] The inset in Fig. 8b shows the equivalent circuit. In the high-frequency range, the intercept represents the sum of ohmic resistance (R_s) of the electrolyte and the electrode. The quasi-semicircle corresponds to the charge transfer resistance (R_{ct}). The constant phase element is associated with the double layer capacitance (CPE). The straight sloping line is ascribed to Warburg impedance (Z_W). According to the equivalent circuit fitting, the charge transfer resistance (R_{ct}) of radial-prisms microspheres is 153.6 Ω, which is much smaller than those of the random-prisms (203.9 Ω) and radial-wedges (224.4 Ω) microspheres. Based on the Warburg equations,[17] Li^+ diffusion coefficients of radial-prisms, random-prisms and radial-wedges microspheres are calculated to be 2.69×10^{-15}, 1.53×10^{-15} and 1.24×10^{-15} cm^2 S^{-1}, respectively. The EIS results make it clear that the radial-prisms microspheres have a smaller charge transfer resistance and a higher Li^+ diffusion coefficient, which agrees well with the above results for the rate capabilities.

The cycling performances of the three microspheres at a rate of 0.2C between 2.4 and 4.5 V for 50 cycles are shown in Fig. 8c. The capacities of the radial-prisms microspheres gradually decrease over the first 10–15 cycles and then tend to stabilize in the subsequent cycles, which still achieves a discharge capacity of 138 mA h g^{-1} with about 94% capacity retention. In contrast, random-prisms microspheres display a discharge capacity of only 121 mA h g^{-1} with *ca.* 91% capacity reservation, and the discharge capacity of radial-wedges microspheres decreases from 119 mA h g^{-1} to 111 mA h g^{-1} after 50 cycles. The obtained results demonstrate that the radial-prisms microspheres have a better cycling stability.

Based on the above results, it can be safely demonstrated that radial-prisms microspheres exhibit an excellent rate capability, which can be attributed to the advantageous structural features of the shells and preferential orientation characteristics of the nanoprisms. Specifically, the well-organized nanoprisms of the radial-prisms microspheres possess abundant radially aligned pore channels. Compared to the irregular pore channels of the random-prisms microspheres, Li^+ accessible channels along the radial direction of the microspheres can evidently ensure faster electrolyte penetration to the interior of the microspheres, which result in higher Li^+ diffusion kinetics.[22,43] Furthermore, the nanoprisms fully expose (010) facets and provide a correspondingly larger proportion of electrochemically active sites for decreasing both Li^+ diffusion flux and iR potential drop, which give rise to a lower electrode polarization across the electrode–electrolyte interface.[38,44] Moreover, the thin thickness along the [010] direction directly reduces the Li^+ migration length from the surface to the center of the nanoprisms, which lead to a more rapid charge transfer.[17,45] As a result, the improvements in the Li^+ diffusion kinetics, electrode polarization and charge transfer during the electrochemical reaction eventually guarantee enhancements to the rate capability of radial-prisms microspheres. Unambiguously, the radially aligned pore channels and the preferred (010) orientation of the radial-prisms microspheres afford the realization of the excellent rate performance. Alternatively, the random-prisms microspheres without the radially aligned pore channels and radial-wedges microspheres with limited active facets exhibit low rate performances.

Additionally, radial-prisms microspheres also demonstrate superior cycle stability. Their well-organized porous shells can gently ease the strains of the volume change due to Li^+ insertion/extraction, which benefits the retention of structural stability, ultimately exhibiting a good cyclability. Meanwhile, the micron-sized morphology of the radial-prisms microspheres with low interfacial energy generally have good fluidity characteristics, and they easily form close packed arrays, which can effectively increase the packing density on the specific area of the current collector, finally enhancing the volumetric energy density of $LiMnPO_4$ based batteries.

Conclusions

In summary, we report a facile solvothermal process to fabricate $LiMnPO_4$ hollow microspheres assembled by radially aligned nanoprisms with fully exposed (010) facets using Li_3PO_4 as the self-sacrificed templates. We also demonstrate that an appropriate change of ammonium based salts in the solvothermal reaction can directly make a difference in the shell structures and subunit orientations. When applied as a cathode for lithium-ion batteries, the nanoprisms-radially assembled microspheres exhibit high rate capabilities. The performance improvements are attributed to the radially aligned pore channels of the shells and the significant preference for the (010) orientation of the nanoprisms, which facilitate rapid electrolyte penetration as well as fast Li^+ insertion.

Conflicts of interest

There are no conflicts to declare.

Acknowledgements

This study was financially supported by the National Natural Science Foundation of China (51564024, 51762022) and the Major Science & Technology Program of Jiangxi Province (20143ACB21024) and the Natural Science Foundation of Jiangxi Province (20171BAB206026) and the Science & Technology Research Program of Jiangxi Provincial Education Department (GJJ150762, GJJ170636) and the Doctoral Starting up Foundation (JZB15005) and "Luling Stars" of Jinggangshan University.

Notes and references

1 J. B. Goodenough and Y. Kim, *Chem. Mater.*, 2010, **22**, 587–603.

2 J. M. Tarascon and M. Armand, *Nature*, 2001, **414**, 359–367.

3 B. L. Ellis, K. T. Lee and L. F. Nazar, *Chem. Mater.*, 2010, **22**, 691–714.

4 Y. Wu, C. Cao, J. Zhang, L. Wang, X. Ma and X. Xu, *ACS Appl. Mater. Interfaces*, 2016, **8**, 19567–19572.

5 L. Zhou, K. Zhang, Z. Hu, Z. Tao, L. Mai, Y. M. Kang, S. L. Chou and J. Chen, *Adv. Energy Mater.*, 2018, **8**, 1701415.

6 D. Choi, D. Wang, I. T. Bae, J. Xiao, Z. Nie, W. Wang, V. V. Viswanathan, Y. J. Lee, J. G. Zhang, G. L. Graff, Z. Yang and J. Liu, *Nano Lett.*, 2010, **10**, 2799–2805.

7 N. H. Kwon, H. Yin, T. Vavrova, J. H. W. Lim, U. Steiner, B. Grobéty and K. M. Fromm, *J. Power Sources*, 2017, **342**, 231–240.

8 X. Xu, T. Wang, Y. Bi, M. Liu, W. Yang, Z. Peng and D. Wang, *J. Power Sources*, 2017, **341**, 175–182.

9 D. Di Lecce, T. Hu and J. Hassoun, *J. Alloys Compd.*, 2017, **693**, 730–737.

10 C. Delacourt, L. Laffont, R. Bouchet, C. Wurm, J. B. Leriche, M. Morcrette, J. M. Tarascon and C. Masquelier, *J. Electrochem. Soc.*, 2005, **152**, A913–A921.

11 G. Wang, Y. Sun, D. Li, W. Wei, X. Feng and K. Müllen, *Small*, 2016, **12**, 3914–3919.

12 X. Hu, X. Sun, M. Yang, H. Ji, X. Li, S. Cai, R. Guo, F. Hou, C. Zheng and W. Hu, *J. Mater. Sci.*, 2017, **52**, 3597–3612.

13 L. Chen, Y. Su, S. Chen, N. Li, L. Bao, W. Li, Z. Wang, M. Wang and F. Wu, *Adv. Mater.*, 2014, **26**, 6756–6760.

14 J. Zeng, Y. Cui, D. Qu, Q. Zhang, J. Wu, X. Zhu, Z. Li and X. Zhang, *ACS Appl. Mater. Interfaces*, 2016, **8**, 26082–26090.

15 L. Wang, X. He, W. Sun, J. Wang, Y. Li and S. Fan, *Nano Lett.*, 2012, **12**, 5632–5636.

16 D. Morgan, A. Van der Ven and G. Ceder, *Electrochem. Solid-State Lett.*, 2004, **7**, A30–A32.

17 L. Peng, X. Zhang, Z. Fang, Y. Zhu, Y. Xie, J. J. Cha and G. Yu, *Chem. Mater.*, 2017, **29**, 10526–10533.

18 X. L. Pan, C. Y. Xu, D. Hong, H. T. Fang and L. Zhen, *Electrochim. Acta*, 2013, **87**, 303–308.

19 Y. K. Sun, S. M. Oh, H. K. Park and B. Scrosati, *Adv. Mater.*, 2011, **23**, 5050–5054.

20 L. Zhou, D. Zhao and X. Lou, *Angew. Chem., Int. Ed.*, 2012, **51**, 239–241.

21 K. Palanisamy, Y. Kim, H. Kim, J. M. Kim and W. S. Yoon, *J. Power Sources*, 2015, **275**, 351–361.

22 J. Jin, S. Z. Huang, J. Shu, H. E. Wang, Y. Li, Y. Yu, L. H. Chen, B. J. Wang and B. L. Su, *Nano Energy*, 2015, **16**, 339–349.

23 Q. Xie, D. Zeng, P. Gong, J. Huang, Y. Ma, L. Wang and D. L. Peng, *Electrochim. Acta*, 2017, **232**, 465–473.

24 Y. Luo, X. Xu, X. Tian, Q. Wei, M. Yan, K. Zhao, X. Xu and L. Mai, *J. Mater. Chem. A*, 2016, **4**, 5075–5080.

25 X. Liu, D. Wu, W. Ji and W. Hou, *J. Mater. Chem. A*, 2015, **3**, 968–972.

26 B. Yan, X. Li, Z. Bai, Y. Zhao, L. Dong, X. Song, D. Li, C. Langford and X. Sun, *Nano Energy*, 2016, **24**, 32–44.

27 X. Y. Yu, X. Z. Yao, T. Luo, Y. Jia, J. H. Liu and X. J. Huang, *ACS Appl. Mater. Interfaces*, 2014, **6**, 3689–3695.

28 S. Hao, B. Zhang, S. Ball, J. Wu, M. Srinivasan and Y. Huang, *J. Mater. Chem. A*, 2016, **4**, 16569–16575.

29 S. Yang, M. Hu, L. Xi, R. Ma, Y. Dong and C. Y. Chung, *ACS Appl. Mater. Interfaces*, 2013, **5**, 8961–8967.

30 L. Zhou, Z. Zhuang, H. Zhao, M. Lin, D. Zhao and L. Mai, *Adv. Mater.*, 2017, **29**, 1602914.

31 N. Lin, T. Li, Y. Han, Q. Zhang, T. Xu and Y. Qian, *ACS Appl. Mater. Interfaces*, 2018, **10**, 8399–8404.

32 J. Li, M. Li, L. Zhang and J. Wang, *J. Mater. Chem. A*, 2016, **4**, 12442–12450.

33 J. Zheng, Y. Cao, C. Cheng, C. Chen, R. W. Yan, H. X. Huai, Q. F. Dong, M. S. Zheng and C. C. Wang, *J. Mater. Chem. A*, 2014, **2**, 19882–19888.

34 L. Yu, H. B. Wu and X. W. Lou, *Adv. Mater.*, 2013, **25**, 2296–2300.

35 K. T. Lee, W. H. Kan and L. F. Nazar, *J. Am. Chem. Soc.*, 2009, **131**, 6044–6045.

36 M. H. Lee, J. Y. Kim and H. K. Song, *Chem. Commun.*, 2010, **46**, 6795–6797.

37 V. S. Saji and H. K. Song, *J. Nanosci. Nanotechnol.*, 2015, **15**, 734–741.

38 L. Wang, F. Zhou and G. Ceder, *Electrochem. Solid-State Lett.*, 2008, **11**, A94–A96.

39 Y. Zhao, L. Peng, B. Liu and G. Yu, *Nano Lett.*, 2014, **14**, 2849–2853.

40 B. Liu, J. Wang, J. Wu, H. Li, Z. Li, M. Zhou and T. Zuo, *J. Mater. Chem. A*, 2014, **2**, 1947–1954.

41 Z. Lou, B. Huang, X. Ma, X. Zhang, X. Qin, Z. Wang, Y. Dai and Y. Liu, *Chem.–Eur. J.*, 2012, **18**, 16090–16096.

42 L. Bao, Y. Chen, G. Xu, T. Yang and Z. Ji, *Eur. J. Inorg. Chem.*, 2018, **2018**, 1533–1539.

43 C. Niu, J. Meng, C. Han, K. Zhao, M. Yan and L. Mai, *Nano Lett.*, 2014, **14**, 2873–2878.

44 G. Xu, Y. Yang, L. Li, F. Li, J. Wang, L. Bao, X. Li, G. Shen and G. Han, *CrystEngComm*, 2016, **18**, 3282–3288.

45 C. A. J. Fisher, V. M. Hart Prieto and M. S. Islam, *Chem. Mater.*, 2008, **20**, 5907–5915.